

## Theoretical exploration of mechanical and superconducting properties of two-dimensional Cairo penta-BP<sub>2</sub>: A first-principles study

Zhiyuan Wen <sup>1,2,\*</sup>, Zheng Liu <sup>3</sup>, Jing Zhu,<sup>1</sup> and Shunhong Zhang <sup>4,†</sup>

<sup>1</sup>National Center for Electron Microscopy in Beijing, School of Materials Science and Engineering, The State Key Laboratory of New Ceramics and Fine Processing, Key Laboratory of Adv. Mater. (MOE), Tsinghua University, Beijing 100084, People's Republic of China

<sup>2</sup>Jihua Laboratory, Foshan 528251, China

<sup>3</sup>Institute for Advanced Study, Tsinghua University, 100084 Beijing, China

<sup>4</sup>International Center for Quantum Design of Functional Materials (ICQD), University of Science and Technology of China, Hefei, 230026 Anhui, China



(Received 28 July 2022; accepted 4 October 2022; published 18 October 2022)

Two-dimensional (2D) Cairo pentagon materials have attracted tremendous interest due to their exotic physical properties. Based on first-principles calculations, we predict that monolayer penta-BP<sub>2</sub> is a promising Cairo pentagon-based 2D material simultaneously harboring a negative Poisson ratio and intrinsic superconductivity. The Poisson ratio exhibits strong anisotropy with alternating positive-negative signs, and its value along the diagonal direction is more negative than that of pentagraphene. The medium-strength coupling between the Fermi-surface electrons and a phonon mode majorly originating from the P<sub>2</sub> dimers leads to a superconducting transition estimated to occur at  $T_c \sim 7.7$  K. Moreover, we find that fluorination/chlorination can efficiently engineer the superconductivity and mechanical properties of penta-BP<sub>2</sub>: achieving higher  $T_c$  of 9.6/10.5 K, turning Poisson's ratio from negative to positive and enhancing Young's modulus. These results render penta-BP<sub>2</sub> an appealing platform to investigate unique superconductivity and mechanical properties in the Cairo pentagon lattice.

DOI: [10.1103/PhysRevMaterials.6.104003](https://doi.org/10.1103/PhysRevMaterials.6.104003)

### I. INTRODUCTION

Two-dimensional (2D) materials have appealed great attention in condensed-matter physics and materials science. Such as their bulk counterparts, 2D materials can host intriguing properties, such as skyrmions [1,2], superconductivity [3], and topological electronic states [4] but with more exotic behavior due to the reduced dimensionality, which is desirable for electronic device miniaturization and related applications. Since the discovery of graphene [5], a wealth of atomic-thick crystalline materials have been experimentally realized, such as hexagonal boron nitride [6], metal carbides, and nitrides [7] and transition-metal dichalcogenides [8]. More recently, thanks to the rapid advances of epitaxial growth techniques, wafer-scale fabrication has been achieved for some monolayer crystalline materials [9,10]. Meanwhile, various approaches have been developed to manipulate their physical properties for optimal applications, such as carrier doping [11–14], strain engineering [15–17], and surface modification [18–20].

Beyond the above-mentioned 2D systems which prototypically possess hexagonal lattice structures, a novel family of pentagon-based 2D materials [21] has also attracted growing interests since the prediction of pentagraphene [22], a buckled

carbon sheet composed exclusively of Cairo pentagon lattice. Such 2D pentagon materials can exhibit extraordinary properties, including the negative Poisson's ratio [22], topological electronic states [23,24], and room-temperature ferromagnetism [25,26]. In recent years, several pentagon based materials, such as penta-Ni<sub>2</sub>N<sub>4</sub> [27] and penta-PdSe<sub>2</sub> [28], have been successfully prepared in experiments, sparking further enthusiasms to devise and synthesize Cairo pentagon tiled materials with tunable properties for vast applications [21,29]. In three-dimensional bulk materials, it has been found that pentagon-based structural motifs formed by light elements are beneficial for emergence of phonon-mediated superconductivity under high pressure [30,31]. However, intrinsic superconductivity in 2D, which is believed to encompass more exotic quantum phenomena due to confined geometry [32,33], has not yet been reported in pentagon-based 2D materials.

Using first-principles calculation, we comprehensively study the electronic, mechanical, and vibrational properties of monolayer penta-BP<sub>2</sub> [34], and predict it as a promising Cairo pentagon based 2D material that simultaneously harbors a negative Poisson's ratio and intrinsic superconductivity. The structural motifs for penta-BP<sub>2</sub>, namely, the BP<sub>4</sub> tetrahedra and P<sub>2</sub> dimers, play important roles respectively in its intriguing mechanical and superconducting properties. The penta-BP<sub>2</sub> monolayer exhibits anisotropic mechanical properties, featured by the negative Poisson's ratio along the diagonal direction, which can be microscopically attributed to the rotation of the corner-sharing BP<sub>4</sub> tetrahedra which tile the Cairo pentagonal geometry. The penta-BP<sub>2</sub> sheet can

\*Author to whom correspondence should be addressed: [zywenphy@163.com](mailto:zywenphy@163.com)

†Author to whom correspondence should be addressed: [szhang2@ustc.edu.cn](mailto:szhang2@ustc.edu.cn)

also be viewed as  $P_2$  dimers interconnected by B atoms. The partially filled  $p_z$  orbitals of these dimers form metallic bands, whereas their vibrations contribute a considerable portion to the electron-phonon coupling (EPC), giving rise to a phonon-mediated superconductivity with the critical transition temperature  $T_c$  of 7.7 K. Furthermore, we investigate the effects of surface modification on the electronic and mechanical properties for penta-BP<sub>2</sub> by introducing fluorine or chlorine atoms. The resultant fluorinated/chlorinated penta-BP<sub>2</sub> are both stable, showing enhanced EPC and higher  $T_c$  as well as a positive Poisson ratio and a larger Young's modulus.

## II. METHODS

The electronic structures, phonon spectra, and EPC are calculated using the QUANTUM ESPRESSO package [35] with norm-conserving pseudopotentials [36] and Perdew-Burke-Ernzerhof (PBE) exchange-correlation functional [37]. The cutoff for kinetic energy and charge density are 100 and 400 Ry, respectively. The structural models are separated from its adjacent periodic images by vacuum layers of 15 and 25 Å for pristine and surface-modified penta-BP<sub>2</sub>, respectively. A Monkhorst-Pack mesh of  $18 \times 18 \times 1$   $k$  points is employed for electronic Kohn-Sham states, and a  $9 \times 9 \times 1$   $q$  mesh is employed for the phonon and EPC calculations implementing the density functional perturbation theory [38]. Superconducting critical temperature  $T_c$  is estimated by the McMillian-Allen-Dynes formula [39–41],

$$T_c = \frac{\omega_{\log}}{1.2} \exp\left[-\frac{1.04(1 + \lambda)}{\lambda - \mu^*(1 + 0.62\lambda)}\right], \quad (1)$$

where  $\mu^*$  is the Coulomb pseudopotential for which we choose a typical value 0.1.  $\lambda$  is the EPC constant, which is calculated from first principles via integrating the Eliashberg spectral function  $\alpha^2F(\omega)$  [39],

$$\lambda = 2 \int \frac{\alpha^2F(\omega)}{\omega} d\omega. \quad (2)$$

The mechanical properties are calculated using the Vienna *ab initio* simulation package (VASP) [42] code and postprocessed using the VASPKIT package [43]. The plane-wave cutoff energy is 540 eV for valence electrons with the projector augmented-wave method [44] and PBE functional [37] implemented for treating the ion core region and the electron exchange correlation, respectively. The Hellman-Feynman force tolerance is 0.01 eV/Å on each ion, and the total energy convergence criteria for the self-consistent calculations is  $10^{-8}$  eV.

## III. RESULTS AND DISCUSSION

### A. Structural and electronic properties

As shown in Fig. 1(a), the top view of penta-BP<sub>2</sub> clearly sketches the beautiful Cairo pentagonal tiling whereas the side view displays buckling of the 2D sheet composed of three atomic layers. Important structural parameters are summarized in Table I. The in-plane (IN) lattice constant is calculated to be  $a = 4.55$  Å, and the buckling between the B layer and one of the P layers is 1.0 Å. Figure 1(b) shows a slightly distorted BP<sub>4</sub> tetrahedron (termed as tetra-BP<sub>4</sub>) which

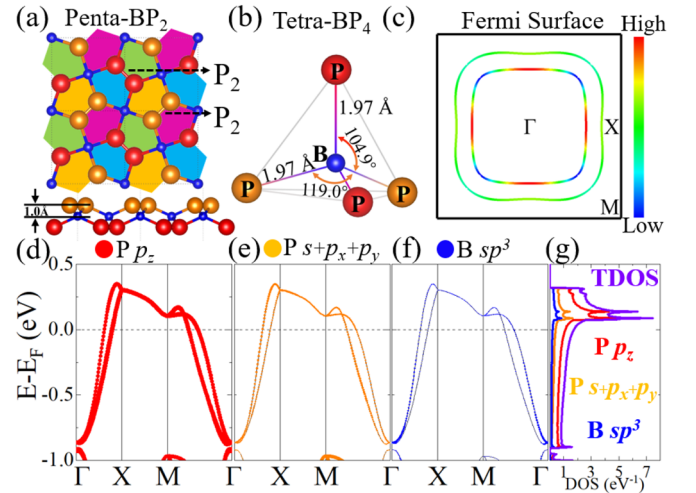


FIG. 1. Crystal and electronic structures for penta-BP<sub>2</sub>. (a) Top and side views of the crystal structure. Blue balls denote B atoms, whereas orange and red balls denote P atoms above and below the B atomic plane, respectively. (b) Structural details of the tetra-BP<sub>4</sub> in penta-BP<sub>2</sub>. (c) Fermi surface in the 2D Brillouin zone. The color bar maps the Fermi velocity. (d)–(f) Band structures and (g) density of states, projected onto  $P p_z$ ,  $P s + p_x + p_y$ , and  $B sp^3$  orbitals, respectively.

constitutes the structural skeleton. The optimized B-P bond length is 1.97 Å, close to that in cubic BP [45]. Assembling of the tetra-BP<sub>4</sub> via sharing corner P atoms leads to formation of  $P_2$  dimers [Fig. 1(a)] with the optimized P-P bond length of 2.16 Å. A simple electron counting can be performed based on such a structure: as a Group-III element, B in a tetra BP<sub>4</sub> can share less than one electron per B-P bond. Consequently, despite the formation of three bonds around each P atom (two B-P bonds and one P-P bond), the P atom does not reach a full shell eight-electron configuration, implying that the compound is a metal.

Figures 1(c)–1(g) show the first-principles Fermi surface, band structures, and density of states (DOS) projected onto

TABLE I. Structural parameters (lattice constants  $a$ , buckling height  $h$ , and characteristic bond lengths) and mechanical properties (elastic constants  $C_{ij}$ , Young's modulus  $E$ , and Poisson ratio  $\nu$ ) for pristine and F<sub>2</sub>BP<sub>2</sub>/Cl<sub>2</sub>BP<sub>2</sub>. The values for  $E_{\min}/E_{\max}$  are distributed along the 0°/45° direction, and those for  $\nu_{\min}/\nu_{\max}$  are distributed along the 45°/90° direction, respectively.

	Penta-BP <sub>2</sub>	F <sub>2</sub> BP <sub>2</sub>	Cl <sub>2</sub> BP <sub>2</sub>
$a$ (Å)	4.55	4.62	4.72
$h$ (Å)	1.00	0.914	0.906
B-P (Å)	1.97	1.95	1.98
P-P (Å)	2.16	2.17	2.22
P-F/Cl (Å)	N/A	1.61	2.08
$C_{11}$ (N/m)	71.8	89.4	99.7
$C_{12}$ (N/m)	8.5	14.4	26.5
$C_{66}$ (N/m)	49.9	47.8	61.1
$E_{\min}/E_{\max}$ (N/m)	70.8/89.1	87.1/99.5	92.6/124.2
$\nu_{\min}/\nu_{\max}$	-0.11/+0.12	0.041/0.16	0.017/0.27

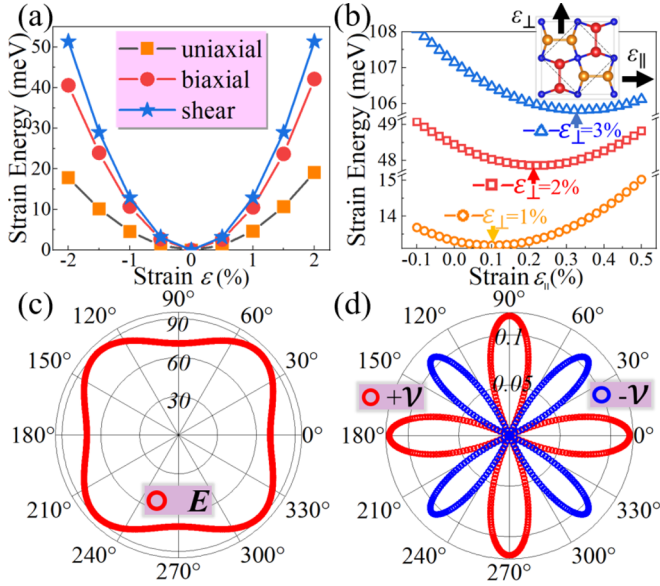


FIG. 2. Mechanical properties of penta-BP<sub>2</sub>. (a) Strain energy under uniaxial, biaxial, and shear strains. (b) Equilibrium energy-strain curves for the  $\sqrt{2} \times \sqrt{2}$  supercell under tensile strain  $\varepsilon_{\perp}$ . The arrows indicate the equilibrium magnitude of strain  $\varepsilon_{\parallel}$ . The inset shows the  $\sqrt{2} \times \sqrt{2}$  supercell model with strain  $\varepsilon_{\perp}$  in the diagonal direction of the primitive cell. Orientation-dependent Young's modulus (c) and Poisson's ratio (d) for penta-BP<sub>2</sub>. Red and blue points denote positive and negative values, respectively.

P  $p_z$ , P  $s + p_x + p_y$ , and B  $sp^3$  orbitals for penta-BP<sub>2</sub>. As expected, the Fermi level is below the P  $p$ -band top, defining two  $\Gamma$ -centered concentric electron pockets on the Fermi surface [Fig. 1(c)] with the inner (outer) one showing an inhomogeneous (homogeneous) distribution of group velocity. The metallic bands mainly stem from the P  $p_z$  orbitals, which is understandable because they have the least hybridization with the B atoms. Consequently, these  $\pi$ -bonding-dominated bands are dispersive and electron deficient. These two metallic bands are well separated from other fully occupied or empty bands and show degeneracy at the Brillouin zone boundary ( $\Gamma$ -X) as protected by the nonsymmorphic screw symmetry [46]. The corresponding density of states exhibit two closely aligned sharp peaks above the Fermi level, signaling clear von Hove singularity which could be utilized for studying electronic instability and pertinent exotic physics upon mild electron doping [47].

### B. Mechanical properties

Next we discuss the mechanical properties of penta-BP<sub>2</sub>. The structural symmetry ( $P\bar{4}_21m$  space group) restricts the elastic tensor to have three independent components, and the elastic energy  $E$  as a function of the strain ( $\varepsilon$ ) can be written as

$$E(\varepsilon) = \frac{1}{2}C_{11}\varepsilon_{xx}^2 + \frac{1}{2}C_{22}\varepsilon_{yy}^2 + C_{12}\varepsilon_{xx}\varepsilon_{yy} + 2C_{66}\varepsilon_{xy}^2, \quad (3)$$

where the strain tensor  $\varepsilon$  has the standard definition, and  $C_{11}$  (equal to  $C_{22}$ ),  $C_{12}$ , and  $C_{66}$  are the three independent elastic constants, following the Voigt notation [48]. Based on the first-principles total energy curves shown in Fig. 2(a),

we obtain the elastic constants  $C_{11} = C_{22} = 71.8$ ,  $C_{12} = 8.5$ , and  $C_{66} = 49.9$  N/m. Thus, the penta-BP<sub>2</sub> structure meets the Born-Huang criteria [49]:  $C_{11} > 0$ ,  $C_{66} > 0$ , and  $C_{11}C_{22} > C_{12}^2$ , which ensures the positive definiteness of the elastic tensor and the mechanical stability of the Cairo pentagonal sheet.

Based on the obtained elastic constants, we further calculate the orientation-dependent Young's modulus  $E$  and Poisson's ratio  $\nu$  using the formulas,

$$E(\theta) = \frac{\Delta C}{C_{11}m^4 + C_{22}n^4 + \left(\frac{\Delta C}{C_{66}} - 2C_{12}\right)m^2n^2}, \quad (4)$$

$$\nu(\theta) = -\frac{(C_{11} + C_{22} - \frac{\Delta C}{C_{66}})m^2n^2 - C_{12}(m^4 + n^4)}{C_{11}m^4 + C_{22}n^4 + \left(\frac{\Delta C}{C_{66}} - 2C_{12}\right)m^2n^2}, \quad (5)$$

where  $\Delta C = C_{11}C_{22} - C_{12}^2$ ,  $m = \cos(\theta)$ , and  $n = \sin(\theta)$  with  $\theta$  being the angle between tensile strain direction and the lattice vector. As shown in Figs. 2(c) and 2(d), the two curves deviated from perfect circles indicate that penta-BP<sub>2</sub> has an anisotropic Young's modulus and Poisson's ratio. Specifically, the Young's modulus  $E$  changes from 70.8 N/m ( $\theta = 0^\circ$ ) to 89.1 N/m ( $\theta = 45^\circ$ ), which is comparable with MoS<sub>2</sub> (129 N/m) [50], Ti<sub>2</sub>C (130 N/m) [51], and silicene (62 N/m) [52]. The magnitude of  $\nu$  varies from  $-0.11$  ( $\theta = 45^\circ$ ) to  $0.12$  ( $\theta = 90^\circ$ ), showing a negative Poisson's ratio (NPR) in the  $xy$  direction. To verify the unexpected NPR, we build a  $\sqrt{2} \times \sqrt{2}$  penta-BP<sub>2</sub> supercell and apply uniaxial tensile strain  $\varepsilon_{\perp}$  along the  $xy$  direction of its primitive cell [Fig. 2(b)]. The transverse strain  $\varepsilon_{\parallel}$  is determined by sweeping the lattice constant along the lateral direction, relaxing the atomic positions, and locating the energy minimum. Poisson's ratio is then calculated by  $\nu = -\frac{\varepsilon_{\parallel}}{\varepsilon_{\perp}}$ . As shown in Fig. 2(b), the transverse strain  $\varepsilon_{\parallel}$  is positive under the tensile strains  $\varepsilon_{\perp}$  of 1%, 2%, and 3%, and the estimated  $\nu$  magnitude is consistent with the most negative value from Eq. (5). These results confirm that penta-BP<sub>2</sub> takes sides in the family of NPR materials, along with the bulk of Cairo pentagon 2D materials. Our detailed analyses by tracing the evolution of the monolayer structure under uniaxial tensile strain (see the Supplemental Material [53]) suggest that the coherent rotation of the corner-sharing tetra-BP<sub>4</sub> motifs is the microscopic origin of the auxetic response in the perpendicular direction. Remarkably, we find that penta-BP<sub>2</sub> has larger NPR than pentagraphene [22], borophene [54], and black phosphorene [55], rendering it a promising auxetic material.

### C. Vibration properties and superconductivity

Now let us discuss the vibrational properties, EPC, and superconductivity of penta-BP<sub>2</sub>. The absence of imaginary mode in the phonon spectra confirms the dynamical stability of penta-BP<sub>2</sub>. By decomposing the phonon bands into the P and B atomic vibrations [Fig. 3(a)], we find that for the low-frequency optical branches from 120 to 170  $\text{cm}^{-1}$ , the vibrations are primarily from the out-of-plane (ON) displacements of the P atoms. In the intermediate-frequency region spanning from 300 to 550  $\text{cm}^{-1}$ , the in-plane vibrations of P atoms constitute these optical branches. The contributions to modes above 550  $\text{cm}^{-1}$  are mainly from the atomic vibrations of the lighter boron.

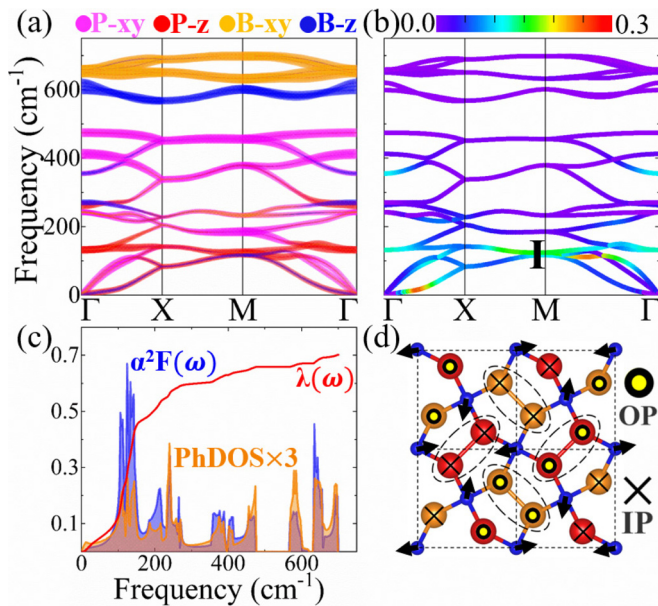


FIG. 3. Vibration properties and electron-phonon coupling for penta-BP<sub>2</sub>. (a) Phonon spectra weighted by the vibrations of P and B atoms. (b) Phonon spectra weighted by the magnitude of EPC  $\lambda_{qv}$ . (c) Phonon density of states (PhDOS), Eliashberg spectral function  $\alpha^2F(\omega)$ , and cumulative frequency-dependent of EPC function  $\lambda(\omega)$ . (d) Vibration mode at point I shown in (b). The symbols IP and OP represent the in-plane (IP) or out-of-plane (OP) directions, respectively.

By integrating the mode- and momentum-dependent EPC  $\lambda_{qv}$  [Fig. 3(b)], we find that penta-BP<sub>2</sub> is a medium-coupling superconductor with  $\lambda$  of 0.7, and the corresponding  $T_c \sim 7.7$  K is higher than that of representative light-element-based 2D materials, such as BeP<sub>2</sub> (1.32 K) [56] and LiC<sub>6</sub> (5.9 K) [57]. The superconductivity-related parameters are summarized in Table II. As shown in Fig. 3(c), the low-frequency range below 170 cm<sup>-1</sup> accounts for 67% of the total EPC. The EPC  $\lambda_{qv}$  around the M point in the frequency range of 110–170 cm<sup>-1</sup> is particularly large, leading to a pronounced peak in the Eliashberg spectral function  $\alpha^2F(\omega)$  [Fig. 3(c)]. Its resonance with the phonon density of states gives rise to a rapid increase in  $\lambda(\omega)$  in this range. We plot the vibration mode with largest  $\lambda_{qv}$  at M point on the second phonon band and identify it as the in-phase vibration of the two P atoms in the P<sub>2</sub> dimers along the out-of-plane direction [Fig. 3(d)]. Apart from the low-frequency region, phonons

TABLE II. Superconductivity-related parameters of pristine and fluorinated/chlorinated penta-BP<sub>2</sub>: the logarithmically averaged phonon frequency  $\omega_{log}$ , density of states at the Fermi level  $N(E_F)$ , electron-phonon coupling coefficient  $\lambda$ , and superconducting transition temperature  $T_c$ .

	Penta-BP <sub>2</sub>	F <sub>2</sub> BP <sub>2</sub>	Cl <sub>2</sub> BP <sub>2</sub>
$\omega_{log}$ (K)	222.1	239.1	286.4
$N(E_F)$ (states/Ry/cell)	23.2	12.4	16.5
$\lambda$	0.7	0.74	0.71
$T_c$ (K)	7.7	9.6	10.5

with medium frequency ranging from 170 to 480 cm<sup>-1</sup> contribute to the total EPC by 26%. The high-frequency phonons above 550 cm<sup>-1</sup> hardly contribute to the EPC.

#### D. Surface-modified penta-BP<sub>2</sub>

Benefited from the large surface-to-volume ratio and the atomically flat geometry and surface modification usually realized via chemical functionalization has been widely utilized to efficiently tailor the physical and mechanical properties of two-dimensional materials [18,19]. Here, we systematically investigate the evolution of structural, electronic, vibrational, superconducting, and mechanical properties of penta-BP<sub>2</sub> monolayer upon surface fluorination or chlorination.

Figures 4(a) and 4(d) show the optimized crystal structures of fully fluorinated/chlorinated penta-BP<sub>2</sub> sheet with the chemical formula of F<sub>2</sub>BP<sub>2</sub>/Cl<sub>2</sub>BP<sub>2</sub>. Primary changes to the lattice structures can be found in Table I. We see a slight increment of the lattice constant in both ternary sheets which could be a compromise during structure relaxation to minimize the repulsive interactions between halogen ions. The buckling height between the B and the P layers is decreased to 0.914 and 0.906 Å, respectively, upon fluorination and chlorination. For the fluorinated/chlorinated penta-BP<sub>2</sub>, the B-P bond length in the tetra-BP<sub>4</sub> is 1.95/1.98 Å, and the P-P bond length in the P<sub>2</sub> dimer is 2.17/2.22 Å, close to those in pristine penta-BP<sub>2</sub>. The P-F and P-Cl bond lengths are, respectively, 1.61 and 2.08 Å, indicating a strong bonding.

Interestingly, unlike fluorographene/chlorographene in which the semimetallicity of the parental graphene is fully suppressed and a moderate band gap is opened [19], the fluorinated/chlorinated penta-BP<sub>2</sub> remains metallic. As shown in Figs. 4(b) and 4(e), both functionalized sheets have two bands crossing the Fermi level, which indeed are still originated from the P *p* orbitals according to our projected DOS analyses. Due to the hybridization with more electronegative halogens, the dispersions of these two bands are drastically altered and the fillings are further diminished, resulting in a significant change to the Fermi-surface topology. The Fermi pockets are now mainly distributed near the Brillouin zone boundary, showing an intriguing feature of interconnected electron and hole pockets (Fig. S2) of the Supplemental Material [53]. The F/Cl atoms have nearly fulfilled closed *p* shell, lying lower in energy, and, therefore, contribute few DOSs at the Fermi level.

Furthermore, we examine the phonon spectra to verify the dynamical stability of fluorinated/chlorinated penta-BP<sub>2</sub> and calculate superconductivity-related parameters following the same recipe, which are summarized in Table II. Apparently, the fluorinated/chlorinated penta-BP<sub>2</sub> are also stable and intrinsically superconductive with slightly enhanced  $\lambda = 0.74/0.71$  and  $T_c = 9.6/10.5$  K. The larger  $T_c$  for the latter is attributed to larger  $N(E_F)$  and  $\omega_{log}$ . To gain more insights into the EPC of fluorinated/chlorinated penta-BP<sub>2</sub>, we calculate their phonon spectra weighted by the magnitude of EPC  $\lambda_{qv}$ . As shown in Figs. 4(c) and 4(f), the EPC for fluorinated penta-BP<sub>2</sub> mainly comes from the low-frequency phonons below 170 cm<sup>-1</sup>, which accounts for 55% of the total EPC. Besides, medium-frequency phonons contribute 39% to the EPC. As for chlorinated penta-BP<sub>2</sub>, the corresponding proportion

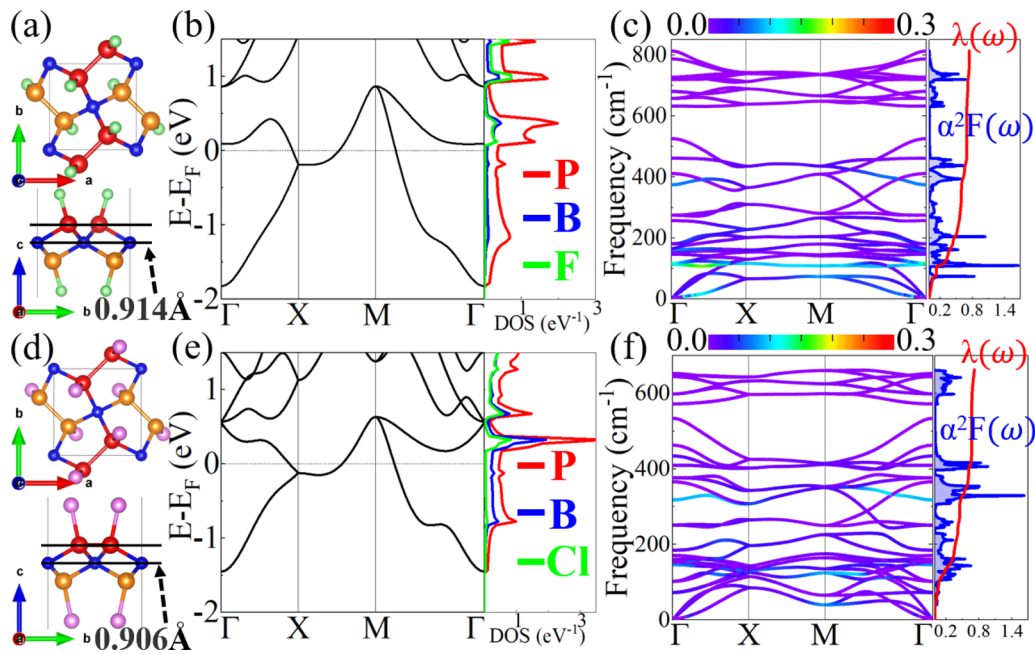


FIG. 4. Effects of surface modification on the physical properties for pena-BP<sub>2</sub>. (a) Crystal structure, (b) band structures and DOS, (c) phonon dispersions weighted by the magnitude of EPC  $\lambda_{qv}$ , Eliashberg function  $\alpha^2F(\omega)$  and EPC function  $\lambda(\omega)$  for fluorinated penta-BP<sub>2</sub>. (d)–(f) Same as (a)–(c) but for chlorinated penta-BP<sub>2</sub>. Green and pink balls denote F and Cl atoms, respectively. The unit of PhDOS is states/cm<sup>-1</sup>/cell.

become 48% and 46%, respectively. Similar to the pristine case, high-energy phonons with frequencies larger than 550 cm<sup>-1</sup> are well separated from other modes by a phonon gap and contribute marginally to the EPC in both decorated sheets.

We also discuss the change of mechanical properties of penta-BP<sub>2</sub> upon surface modification. By calculating the

strain-energy curves [Figs. 5(a) and 5(d)] and fitting them with Eq. (3), the elastic constants are obtained and listed in Table I. One can see that the 2D pentasheet is, in general, stiffened upon surface functionalization except for the shear modulus of fluorinated penta-BP<sub>2</sub> showing a slight weakening. We again calculate the orientation-dependent Young's modulus  $E(\theta)$  and Poisson's ratio  $\nu(\theta)$  using Eqs. (4) and (5). As shown in

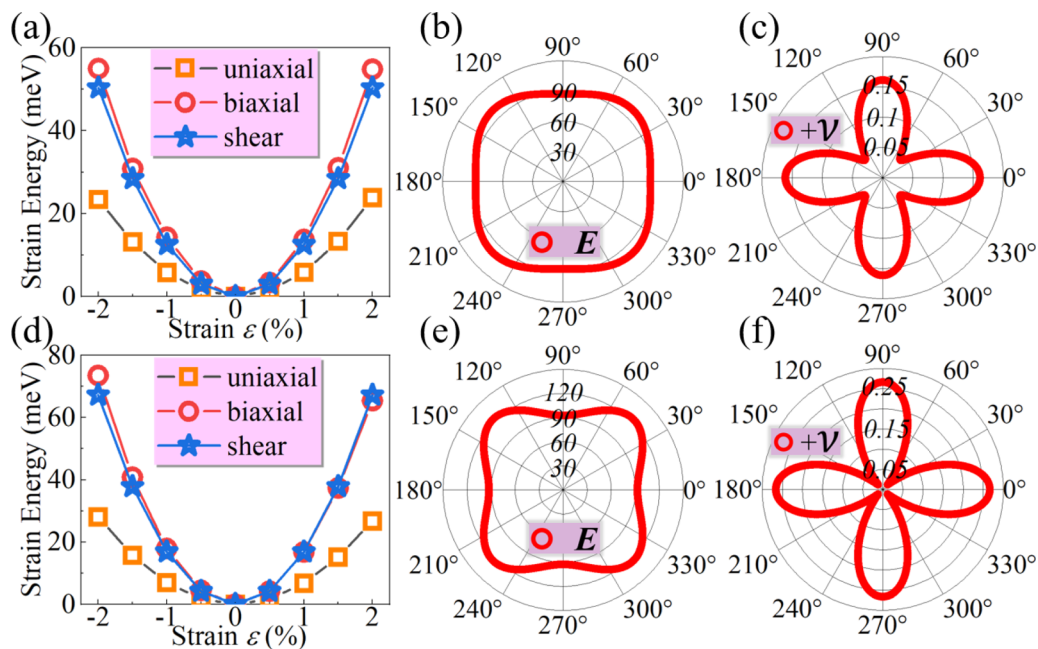


FIG. 5. Mechanical properties of surface-modified penta-BP<sub>2</sub>. (a) Strain energy under uniaxial, biaxial, and shear strains, (b) orientation-dependent Young's modulus, and (c) Poisson's ratio of fluorinated penta-BP<sub>2</sub>. (d)–(f) the same as (a)–(c) but for chlorinated penta-BP<sub>2</sub>.

Figs. 5(b) and 5(e), the Young's modulus  $E(\theta)$  varies from 87.1 N/m ( $\theta = 0^\circ$ ) to 99.5 N/m ( $\theta = 45^\circ$ ) for fluorinated penta-BP<sub>2</sub> and from 92.6 N/m ( $\theta = 0^\circ$ ) to 124.2 N/m ( $\theta = 45^\circ$ ) for chlorinated penta-BP<sub>2</sub>. The enlarged Young's modulus for surface-modified penta-BP<sub>2</sub> could be attributed to the different bond characteristics which will be discussed later. As sketched in Figs. 5(c) and 5(f), when  $\theta$  increases from  $0^\circ$  to  $45^\circ$ , Poisson's ratio  $\nu$  decreases monotonically from 0.16 (0.27) to 0.041 (0.017) for fluorinated (chlorinated) penta-BP<sub>2</sub>, still exhibit strong anisotropy, but the minimum values become positive, indicating that the NPR feature of pristine penta-BP<sub>2</sub> is fully suppressed in both cases, similar to previously studied functionalized pentagraphene [19].

Before closing, we present more detailed analysis on the covalency-ionicity interplay of chemical bonds [58] in penta-BP<sub>2</sub> as well as the changes upon surface modification and discuss their effects on the superconducting and mechanical properties. In doing so, we have calculated the electron localized function (ELF) [59], integrated local density of states (ILDOS), and projected crystal orbital Hamilton population (pCOHP) [60] of pristine and fluorinated/chlorinated penta-BP<sub>2</sub> monolayers and summarized the results in the Supplemental Material, Fig. S3 [53]. According to the ELF mapping in Figs. S3(a<sub>1</sub>)–S3(a<sub>3</sub>) in the Supplemental Material [53], the B-P and P-P bonds in both pristine and functionalized monolayers possess typical covalent nature with the highly localized electrons mainly accumulated in the central region of the bonds. The P-X ( $X = \text{F/Cl}$ ) bonds, in contrast, exhibit ionic feature as signified by the polar distribution of the bonding electrons, which mostly exist as lone pair in the pristine monolayer. To further investigate the electronic states dominating the superconductivity, we integrate the local density of states within the energy window of  $[E_f - 0.5 \text{ eV}, E_f]$ . As shown in Figs. S3(b<sub>1</sub>)–S3(b<sub>3</sub>) of the Supplemental Material [53], the metallic bands of pristine penta-BP<sub>2</sub> are dominated by the lone pair of electrons of P, featured by the large localized ILDOS. In the halogenated monolayers, this portion of charge mostly transfers to the X ions upon formation of P-X bonds, and the low-energy states are majorly originated from the B-P and P-P bonds, leading to a more spread distribution of ILDOS which partially accounts for the slightly higher  $T_c$ . By inspecting the pCOHP profiles in Figs. S3(c<sub>1</sub>)–S3(c<sub>3</sub>) of the Supplemental Material [53], we also found significant

changes upon surface modification. The antibonding states of P-P bonds are pushed away from the Fermi level due to the passivation of the lone pair electrons. For the B-P bonds which largely dictates the in-plane stiffness, some antibonding states arise right above the Fermi level in halogenated monolayers, indicating potential strengthening consistent with our elastic constant calculations.

#### IV. SUMMARY

To summarize, we predict that the two-dimensional penta-BP<sub>2</sub> has negative Poisson's ratio along the diagonal direction and is an intrinsic medium-coupling superconductor. Different from most Cairo pentagon tiled 2D covalent networks which exhibit large insulating gap, penta-BP<sub>2</sub> is metallic with two partially filled dispersive bands mainly from the conjugated P  $p_z$  orbitals. The in-phase vibration of the two P atoms in the P<sub>2</sub> dimers along the out-of-plane direction contributes to the major part of electron-phonon coupling, giving rise to a superconducting state under  $T_c$  of 7.7 K. Furthermore, we find that fluorination and chlorination can enhance the EPC of penta-BP<sub>2</sub> and achieve higher  $T_c$  of 9.6 and 10.5 K, respectively. Surface functionalization also significantly manipulates the mechanical properties of penta-BP<sub>2</sub> in terms of enhanced Young's modulus and suppressed negative Poisson's ratio. These findings would stimulate more interest on the exploration of Cairo pentagonal superconductors and provide valuable insight into the engineering of the physical properties for other Cairo pentagonal 2D materials.

#### ACKNOWLEDGMENTS

This work was financially supported by the Chinese National Natural Science Foundation (Basic Science Center Project of NSFC under Grant No. 51788104) and supported by the Basic and Applied Basic Research Major Programme of Guangdong Province, China (Grant No. 2021B0301030003), and Jihua Laboratory (Project No. X210141TL210). S.Z. acknowledges support from the National Natural Science Foundation (Grant No. 11904350) and Anhui Provincial National Natural Science Foundation (Grant No. 2008085QA30). This work made use of the resources of the National Center for Electron Microscopy in Beijing.

- 
- [1] J. Yuan, Y. Yang, Y. Cai, Y. Wu, Y. Chen, X. Yan, and L. Shen, *Phys. Rev. B* **101**, 094420 (2020).
- [2] B. Li, J.-Q. Yan, D. M. Pajerowski, E. Gordon, A.-M. Nedić, Y. Sizyuk, L. Ke, P. P. Orth, D. Vahnin, and R. J. McQueeney, *Phys. Rev. Lett.* **124**, 167204 (2020).
- [3] J. Bekaert, M. Petrov, A. Aperis, P. M. Oppeneer, and M. V. Milošević, *Phys. Rev. Lett.* **123**, 077001 (2019).
- [4] Y. Xu, B. Yan, H. J. Zhang, J. Wang, G. Xu, P. Tang, W. Duan, and S. C. Zhang, *Phys. Rev. Lett.* **111**, 136804 (2013).
- [5] K. S. Novoselov, A. K. Geim, S. V. Morozov, D. Jiang, Y. Zhang, S. V. Dubonos, I. V. Grigorieva, and A. A. Firsov, *Science* **306**, 666 (2004).
- [6] G. Lu, T. Wu, Q. Yuan, H. Wang, H. Wang, F. Ding, X. Xie, and M. Jiang, *Nat. Commun.* **6**, 6160 (2015).
- [7] M. Naguib, V. N. Mochalin, M. W. Barsoum, and Y. Gogotsi, *Adv. Mater.* **26**, 992 (2014).
- [8] S. Manzeli, D. Ovchinnikov, D. Pasquier, O. V. Yazyev, and A. Kis, *Nat. Rev. Mater.* **2**, 17033 (2017).
- [9] J. Wang, X. Xu, T. Cheng, L. Gu, R. Qiao, Z. Liang, D. Ding, H. Hong, P. Zheng, Z. Zhang, Z. Zhang, S. Zhang, G. Cui, C. Chang, C. Huang, J. Qi, J. Liang, C. Liu, Y. Zuo, G. Xue, X. Fang, J. Tian, M. Wu, Y. Guo, Z. Yao, Q. Jiao, L. Liu, P. Gao, Q. Li, R. Yang, G. Zhang, Z. Tang, D. Yu, E. Wang, J. Lu, Y. Zhao, S. Wu, F. Ding, and K. Liu, *Nat. Nanotechnol.* **17**, 33 (2022).

- [10] L. Wang, X. Xu, L. Zhang, R. Qiao, M. Wu, Z. Wang, S. Zhang, J. Liang, Z. Zhang, Z. Zhang, W. Chen, X. Xie, J. Zong, Y. Shan, Y. Guo, M. Willinger, H. Wu, Q. Li, W. Wang, P. Gao, S. Wu, Y. Zhang, Y. Jiang, D. Yu, E. Wang, X. Bai, Z. Wang, F. Ding, and K. Liu, *Nature (London)* **570**, 91 (2019).
- [11] C. Cheng, J. T. Sun, H. Liu, H. X. Fu, J. Zhang, X. R. Chen, and S. Meng, *2D Mater.* **4**, 025032 (2017).
- [12] L. Yan, T. Bo, W. Zhang, P. F. Liu, Z. Lu, Y. G. Xiao, M. H. Tang, and B. T. Wang, *Phys. Chem. Chem. Phys.* **21**, 15327 (2019).
- [13] J. Ye, Y. J. Zhang, R. Akashi, M. S. Bahramy, R. Arita, and Y. Iwasa, *Science* **338**, 1193 (2012).
- [14] J. Lu, O. Zheliuk, I. Leermakers, N. F. Yuan, U. Zeitler, K. T. Law, and J. Ye, *Science* **350**, 1353 (2015).
- [15] C. Si, Z. Liu, W. Duan, and F. Liu, *Phys. Rev. Lett.* **111**, 196802 (2013).
- [16] L. Yan, T. Bo, P. F. Liu, L. Zhou, J. Zhang, M. H. Tang, Y. G. Xiao, and B. T. Wang, *J. Mater. Chem. C* **8**, 1704 (2020).
- [17] J. Cenker, S. Sivakumar, K. Xie, A. Miller, P. Thijssen, Z. Liu, A. Dismukes, J. Fonseca, E. Anderson, X. Zhu, X. Roy, D. Xiao, J. H. Chu, T. Cao, and X. Xu, *Nat. Nanotechnol.* **17**, 256 (2022).
- [18] J. T. Robinson, J. S. Burgess, C. E. Junkermeier, S. C. Badescu, T. L. Reinecke, F. Keith Perkins, M. K. Zalalutdniov, J. W. Baldwin, J. C. Culbertson, P. E. Sheehan, and E. S. Snow, *Nano Lett.* **10**, 3001 (2010).
- [19] X. Li, S. Zhang, F. Q. Wang, Y. Guo, J. Liu, and Q. Wang, *Phys. Chem. Chem. Phys.* **18**, 14191 (2016).
- [20] D. C. Elias, R. R. Nair, T. M. G. Mohiuddin, S. V. Morozov, P. Blake, M. P. Halsall, A. C. Ferrari, D. W. Boukhvalov, M. I. Katsnelson, A. K. Geim, and K. S. Novoselov, *Science* **323**, 610 (2009).
- [21] M. A. Nazir, A. Hassan, Y. Shen, and Q. Wang, *Nano Today* **44**, 101501 (2022).
- [22] S. Zhang, J. Zhou, Q. Wang, X. Chen, Y. Kawazoe, and P. Jena, *Proc. Natl. Acad. Sci. USA* **112**, 2372 (2015).
- [23] S. Bravo, M. Pacheco, V. Nuñez, J. Correa, and L. Chico, *Nanoscale* **13**, 6117 (2021).
- [24] Y. Ma, L. Kou, X. Li, Y. Dai, and T. Heine, *NPG Asia Mater.* **8**, e264 (2016).
- [25] K. Zhang, M. Chen, D. Wang, H. Lv, X. Wu, and J. Yang, *Nanoscale* **13**, 19493 (2021).
- [26] K. Zhao and Q. Wang, *Appl. Surf. Sci.* **505**, 144620 (2020).
- [27] M. Bykov, E. Bykova, A. V. Ponomareva, F. Tasnádi, S. Chariton, V. B. Prakapenka, K. Glazyrin, J. S. Smith, M. F. Mahmood, I. A. Abrikosov, and A. F. Goncharov, *ACS Nano* **15**, 13539 (2021).
- [28] A. D. Oyedele, S. Yang, L. Liang, A. A. Puzetzy, K. Wang, J. Zhang, P. Yu, P. R. Pudasaini, A. W. Ghosh, Z. Liu, C. M. Rouleau, B. G. Sumpter, M. F. Chisholm, W. Zhou, P. D. Rack, D. B. Geohegan, and K. Xiao, *J. Am. Chem. Soc.* **139**, 14090 (2017).
- [29] Y. Shen and Q. Wang, *Phys. Rep.* **964**, 1 (2022).
- [30] H. Xie, Y. Yao, X. Feng, D. Duan, H. Song, Z. Zhang, S. Jiang, S. A. T. Redfern, V. Z. Kresin, C. J. Pickard, and T. Cui, *Phys. Rev. Lett.* **125**, 217001 (2020).
- [31] Q. Yang, K. Zhao, H. Liu, and S. Zhang, *J. Phys. Chem. Lett.* **12**, 5850 (2021).
- [32] Y. Saito, T. Nojima, and Y. Iwasa, *Nat. Rev. Mater.* **2**, 16094 (2017).
- [33] C. Brun, T. Cren, and D. Roditchev, *Supercond. Sci. Technol.* **30**, 013003 (2016).
- [34] L. Wang, L. Jin, G. Liu, Y. Liu, X. Dai, and X. Zhang, *Appl. Mater. Today* **23**, 101057 (2021).
- [35] P. Giannozzi, S. Baroni, N. Bonini, M. Calandra, R. Car, C. Cavazzoni, D. Ceresoli, G. L. Chiarotti, M. Cococcioni, I. Dabo, A. D. Corso, S. Gironcoli, S. Fabris, G. Fratesi, R. Gebauer, U. Gerstmann, C. Gougoussis, A. Kokalj, M. Lazzeri, L. Martin-Samos, N. Marzari, F. Mauri, R. Mazzarello, S. Paolini, A. Pasquarello, L. Paulatto, C. Sbraccia, S. Scandolo, G. Sclauzero, A. Seitsonen, A. Smogunov, P. Umari, and R. Wentzcovitch, *J. Phys.: Condens. Matter* **21**, 395502 (2009).
- [36] D. R. Hamann, *Phys. Rev. B* **88**, 085117 (2013).
- [37] J. P. Perdew, K. Burke, and M. Ernzerhof, *Phys. Rev. Lett.* **77**, 3865 (1996).
- [38] S. Baroni, S. De Gironcoli, A. Dal Corso, and P. Giannozzi, *Rev. Mod. Phys.* **73**, 515 (2001).
- [39] W. McMillan, *Phys. Rev.* **167**, 331 (1968).
- [40] R. Dynes, *Solid State Commun.* **10**, 615 (1972).
- [41] P. B. Allen and R. Dynes, *Phys. Rev. B* **12**, 905 (1975).
- [42] G. Kresse and J. Furthmüller, *Phys. Rev. B* **54**, 11169 (1996).
- [43] V. Wang, N. Xu, J. C. Liu, G. Tang, and W. T. Geng, *Comput. Phys. Commun.* **267**, 108033 (2021).
- [44] P. E. Blöchl, *Phys. Rev. B* **50**, 17953 (1994).
- [45] V. L. Solozhenko and S. F. Matar, *J. Mater. Chem. C* **10**, 3937 (2022).
- [46] S. Zhang, J. Zhou, Q. Wang, and P. Jena, *J. Phys. Chem. C* **120**, 3993 (2016).
- [47] P. Rosenzweig, H. Karakachian, D. Marchenko, K. Küster, and U. Starke, *Phys. Rev. Lett.* **125**, 176403 (2020).
- [48] R. C. Andrew, R. E. Mapasha, A. M. Ukpong, and N. Chetty, *Phys. Rev. B* **85**, 125428 (2012).
- [49] Y. Ding and Y. Wang, *J. Phys. Chem. C* **117**, 18266 (2013).
- [50] R. C. Cooper, C. Lee, C. A. Marianetti, X. Wei, J. Hone, and J. W. Kysar, *Phys. Rev. B* **87**, 035423 (2013).
- [51] S. Wang, J. X. Li, Y. L. Du, and C. Cui, *Comput. Mater. Sci.* **83**, 290 (2014).
- [52] M. Topsakal and S. Ciraci, *Phys. Rev. B* **81**, 024107 (2010).
- [53] See Supplemental Material at <http://link.aps.org/supplemental/10.1103/PhysRevMaterials.6.104003> for the effects of tensile strain on the crystal structure of penta-BP<sub>2</sub>, Fermi surfaces of the fluorinated/chlorinated penta-BP<sub>2</sub>, electron localization function, integrated local density of states, and projected crystal orbital Hamilton population.
- [54] A. J. Mannix, X. Zhou, B. Kiraly, J. D. Wood, D. Alducin, B. D. Myers, X. Liu, B. L. Fisher, U. Santiago, J. R. Guest, M. J. Yacaman, A. Ponce, A. R. Oganov, M. C. Hersam, and N. P. Guisinger, *Science* **350**, 1513 (2015).
- [55] J. W. Jiang and H. S. Park, *Nat. Commun.* **5**, 4727 (2014).
- [56] L. Hengtao, H. Wang, L. Yan, X. Li, Y. Chen, and H. Wang, *Phys. Chem. Chem. Phys.* **23**, 12834 (2021).
- [57] J. J. Zheng and E. R. Margine, *Phys. Rev. B* **94**, 064509 (2016).
- [58] A. Kartsev, S. Malkovsky, and A. Chibisov, *Nanomaterials* **11**, 2967 (2021).
- [59] A. D. Becke and K. E. Edgecombe, *J. Chem. Phys.* **92**, 5397 (1990).
- [60] V. L. Deringer, A. L. Tchougréeff, and R. Dronskowski, *J. Phys. Chem. A* **115**, 5461 (2011).